Article

Investigating the Impact of Local Manipulations on Spontaneous and Evoked Brain Complexity Indices: A Large-Scale Computational Model

Gianluca Gaglioti [1,2,*,†], Thierry Ralph Nieus [3,*,†], Marcello Massimini [1,4,5] and Simone Sarasso [1]

1. Department of Biomedical and Clinical Sciences, University of Milan, 20157 Milan, Italy; marcello.massimini@unimi.it (M.M.); simone.sarasso@unimi.it (S.S.)
2. Department of Philosophy 'Piero Martinetti', University of Milan, 20122 Milan, Italy
3. Core Facility Indaco, University of Milan, 20122 Milan, Italy
4. IRCCS Fondazione Don Carlo Gnocchi ONLUS, 20162 Milan, Italy
5. Azrieli Program in Brain, Mind and Consciousness, Canadian Institute for Advanced Research, Toronto, ON M5G 1M1, Canada
* Correspondence: gianluca.gaglioti@unimi.it (G.G.); thierry.nieus@unimi.it (T.R.N.)
† These authors contributed equally to this work.

Abstract: Brain complexity relies on the integrity of structural and functional brain networks, where specialized areas synergistically cooperate on a large scale. Local alterations within these areas can lead to widespread consequences, leading to a reduction in overall network complexity. Investigating the mechanisms governing this occurrence and exploring potential compensatory interventions is a pressing research focus. In this study, we employed a whole-brain in silico model to simulate the large-scale impact of local node alterations. These were assessed by network complexity metrics derived from both the model's spontaneous activity (i.e., Lempel–Ziv complexity (LZc)) and its responses to simulated local perturbations (i.e., the Perturbational Complexity Index (PCI)). Compared to LZc, local node silencing of distinct brain regions induced large-scale alterations that were paralleled by a systematic drop of PCI. Specifically, while the intact model engaged in complex interactions closely resembling those obtained in empirical studies, it displayed reduced PCI values across all local manipulations. This approach also revealed the heterogeneous impact of different local manipulations on network alterations, emphasizing the importance of posterior hubs in sustaining brain complexity. This work marks an initial stride toward a comprehensive exploration of the mechanisms underlying the loss and recovery of brain complexity across different conditions.

Keywords: brain complexity; whole-brain modeling; node silencing; perturbations; Lempel–Ziv complexity; Perturbational Complexity Index

1. Introduction

Over the years, the concept of brain complexity has gained traction within neuroscientific research. In this general framework, brain networks strike an optimal balance between the requirement for functional specialization (differentiation) and that for tight interactions (integration) across modules [1–3]. Within a continuum ranging from segregated subsystems to an entirely homogeneous macrosystem, the brain would fall in between, in a complex regime where functionally differentiated groups of neurons are able to engage in tight reciprocal interactions so that the whole is more than the sum of its parts [4,5].

Recently, this theoretical notion has drawn extensive empirical attention with several human and animal studies proposing empirical estimates of brain complexity [6]. Specifically, a growing body of experimental literature has demonstrated a reliable correlation between complexity measures and the presence or absence of consciousness across different conditions, confirming early theoretical principles [7].

Recently, structural human brain networks, also known as 'connectomes' [8,9], became available thanks to different initiatives like the Human Connectome Project and the UK Biobank Imaging project [10–12]. When such networks are endowed with mathematical models of local excitability in each node, they allow the development of computational models to simulate whole-brain dynamics [13–15]. These models provide a controlled and mechanistic framework to explore a broad spectrum of parameters that are potentially relevant for better understanding global brain properties such as those implicated in brain complexity [2,16].

Most empirical and computational investigations have explored network complexity based on spontaneous neural activity [6]. Such an observational approach can be usefully complemented by a causal approach, whereby stimulations are used to assess the complexity of neuronal interactions from a causal, rather than correlational, perspective. Along these lines, the Perturbational Complexity Index (PCI) [17] empirically estimates the joint presence of differentiation and integration by quantifying the richness of the spatiotemporal patterns of cortical activity extracted from the electroencephalographic (EEG) response to a brief local perturbation with transcranial magnetic stimulation (TMS). PCI has provided a reliable index to assess the loss and recovery of consciousness in both physiological and pathological conditions [18]. Supported by a series of multiscale experiments in cell cultures [19,20], cortical slices [21], animal models [22–24], and intracranial and extracranial human studies [17,18,25–29], this perturb-and-measure approach has also recently been applied in silico. This computational neuroscience implementation can further elucidate the mechanistic link between brain complexity and anatomic-physiological brain properties. Specifically, the relationship between brain complexity and structural connectivity [30,31] as well as functional network properties [32] have been investigated. In addition, the modulations of brain complexity dependent on global neuromodulation [33] as well as local node properties [34] have been recently addressed.

Crucially, it is also possible to link single node properties to large-scale network dynamics [35,36] and explore the global effects of local manipulations, such as virtual lesions [37] and silencing [38].

Previous computational investigations have shown that large-scale spontaneous network dynamics change considerably upon local connectivity alterations (i.e., local node deletion within spatially defined regions) [39]. Along these lines, a strong reduction of brain-wide activity was observed particularly when simulating the regional inactivation of posterior areas [40]. These results are particularly relevant in view of a postulated critical role of posterior regions of the cortex [41,42] in supporting complexity and consciousness. So far, however, computational studies relating local properties to global brain states have focused mostly on spontaneous activity [37] and have not explored the complexity of neuronal interaction from a causal perspective (i.e., using controlled model perturbations).

Here, we exploited direct perturbations and investigated the large-scale impact of controlled local manipulations (i.e., local node silencing) on network activity and brain complexity in a whole-brain computational model. Specifically, using "The Virtual Brain" platform [13,43], we extensively and systematically varied the topology of the stimulated and the silenced nodes and performed a direct comparison between metrics derived from observational (Lempel–Ziv complexity) [44] and perturbational approaches (PCI). In addition, we explored critical properties governing the network information flow [45] and linked specific features of network organization (i.e., integration and segregation) to the above-mentioned network complexity metrics.

Our intact model exhibited complex spontaneous patterns emerging from the structural links of the connectome and engaged in complex and enduring cortical interactions following focal exogenous perturbations closely resembling the empirical TMS-EEG responses. Importantly, node manipulations revealed an overall reduction of network complexity measures, underlining interesting dissociations between observational and perturbational metrics. Interestingly, the impact of local manipulations was highly heterogeneous, and the comprehensive spatial sampling of the implemented node silencing

allowed assessing relevant regional aspects with respect to the role of posterior cortical regions for brain complexity.

Overall, our results aim at better characterizing the effects of local manipulations on large-scale network dynamics and may serve as a useful tool to systematically assess the mechanisms underlying the loss and recovery of brain complexity in pathological conditions.

2. Materials and Methods

2.1. Model Simulations

2.1.1. Structural Connectivity

For the main results of this study, we employed a connectome composed of 76 areas available in the TVB simulator (2.7.2) (named "Default" connectome, Dconn). Dconn is based on an anatomical tracing reconstruction (CoCoMac) [46] with directional connections and is therefore well suited to investigate propagating activities in brain networks [47]. Additionally, we implemented a subset of analyses on a connectome with finer parcellation consisting of 998 areas (named "Hagmann" connectome, Hconn [48]), as described in Section 2.1.5.

2.1.2. Neural Mass Model

To model the mesoscopic dynamics of cortical regions, we used the Larter and Breakspear model [49], a conductance-based neural mass model widely employed for simulating whole-brain dynamics in intact networks [50–58] and lesioned networks [39,59]. According to the model, the dynamics of a node k are governed by the following ordinary differential equations (ODEs):

$$
\begin{aligned}
\frac{dV^k}{dt} = &-\left(g_{Ca} + (1-C)\,r_{NMDA}\,a_{ee}\,Q_V + C\,r_{NMDA}\,a_{ee}\,Q_V^{network}\right) m_{Ca}(V - V_{Ca}) \\
&-\left(g_{Na}\,m_{Na} + (1-C)\,a_{ee}\,Q_V + C\,a_{ee}\,Q_V^{network}\right)(V - V_{Na}) \\
&- g_K W(V - V_K) - g_L(V - V_L) - a_{ie}\,Z\,Q_Z + a_{ne}I
\end{aligned}
\tag{1}
$$

$$
\frac{dZ^k}{dt} = b(a_{ni}I + a_{ie}\,V\,Q_V)
\tag{2}
$$

$$
\frac{dW^k}{dt} = \frac{\Phi(m_K - W)}{\tau_K}
\tag{3}
$$

where V is the mean membrane potential of the excitatory pyramidal neurons, Z is the mean membrane potential of the inhibitory interneurons, and W is the average number of open potassium ion channels. The term r_{NMDA} is the ratio of NMDA receptors to AMPA receptors, and a_{xy} is the synaptic strength originating from population x (e.g., e, i, n, where e refers to the excitatory population, i to the inhibitory one, and n denotes a nonspecific input) to population y (e.g., e, i). The rate terms b and ϕ govern the time scales of Z and W, respectively. The term g_{ion} is the maximum conductance (i.e., when all channels are open) of the corresponding ion species. The voltage-dependent fractions of open channels for a given ion is determined by m_{ion} and is modeled by a sigmoidal shape function:

$$
m_{ion} = 0.5\left(1 + \tanh\left(\frac{V - T_{ion}}{\delta_{ion}}\right)\right)
\tag{4}
$$

where T_{ion} is the mean threshold membrane potential of a given ion channel population, and δ_{ion} is its standard deviation. The mean firing rates of the excitatory and inhibitory populations are determined by the voltage-dependent activation functions Q_V and Q_Z, respectively, modeled as:

$$
Q_V = 0.5\,Q_{Vmax}\left(1 + \tan h\left(\frac{V - V_T}{\delta_V}\right)\right)
\tag{5}
$$

$$Q_Z = 0.5\, Q_{Zmax} \left(1 + \tanh\left(\frac{V - Z_T}{\delta_{Zq}}\right)\right) \tag{6}$$

where QV_{max} and QZ_{max} are the maximum firing rates of the excitatory and inhibitory populations, respectively. Their corresponding thresholds for action potential generation are given by the terms V_T and Z_T, with standard deviations δ_V and δ_Z, respectively. The network input to node k is given by:

$$Q_V^{network} = \sum_j G\, u_{kj} Q_V \left(V_j\left(t - \tau_{kj}\right)\right) \tag{7}$$

where u_{kj} is the connection weight from node j to node k, τ is the input delay time, and G is the global coupling that scales the connection weights. The parameter C in Equation (1) ranges within [0, 1] and balances the strength of the self-connections against those of the rest of the network.

The ODEs were solved starting from random initial conditions with the stochastic Heun integration method available in TVB (with additive Gaussian noise, standard deviation SD = 10^{-7}) and an integration time step of 0.1 ms. A pre-processing step was performed to reduce the amount of data by temporally resampling the data to a resolution time of 1 ms (i.e., averaging over each 1 ms time step). In addition, the first 3 s of simulations were discarded (first 14 s in Hconn) to remove the initial transient activities in the model.

In order to improve the responsiveness of the nodes (e.g., propagating activities) to stimulation, we varied a set of parameters (indicated in bold in Table S2) with respect to other studies that investigated only the model's spontaneous activity (e.g., [39]). In addition, we set the global coupling G (Equation (7)) in such a way as to maximize the overlap between the functional and the structural connectivity (Figure 1c, see also [60]).
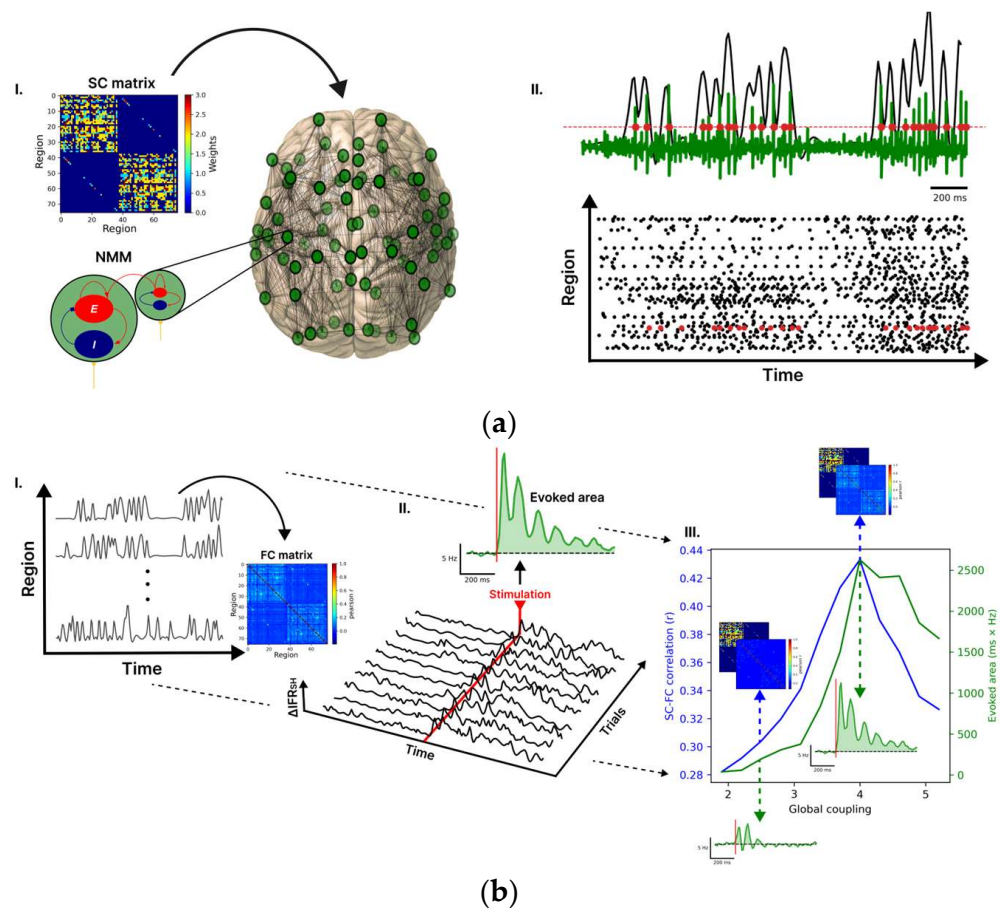

(a)

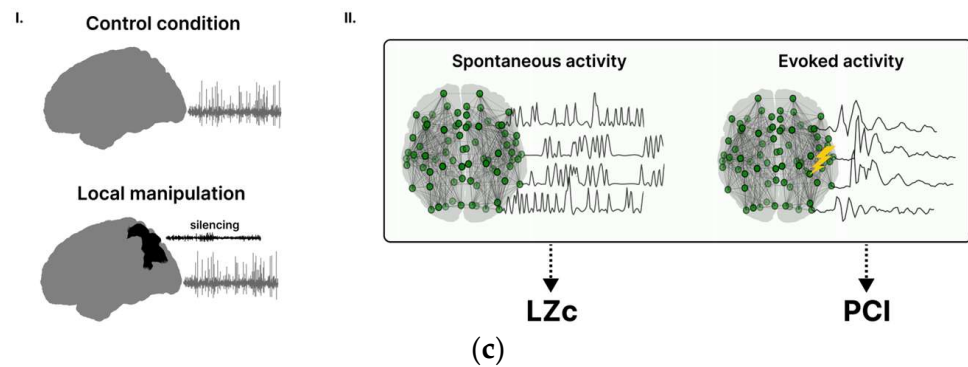
(b)

Figure 1. *Cont.*

Figure 1. Whole-brain model for investigating brain complexity in silico. (**aI**) Each node of the whole-brain network is modelled by the Larter and Breakspear (LB) neural mass model (NMM), describing the interaction between excitatory (E) and inhibitory (I) neurons. The weights connecting the nodes are reported in the structural connectivity (SC) matrix. (**aII**) The output of the model of a given node is the mean membrane potential of the excitatory population (green trace), and the timing of the spikes (red dots), detected with a hard threshold on the voltage, are then converted to an instantaneous firing rate (IFR) (black overlay trace). (**b**) The working point of the model (i.e., set of model parameters) was obtained based on the spontaneous and evoked activity following three steps. First (**bI**), the correlations between the spontaneous IFR traces were computed to estimate a functional connectivity (FC) matrix. Then, the similarity between the FC and SC matrices was assessed through the Pearson correlation coefficient. Second (**bII**), by stimulating a node of the connectome (here rPCi), the propagation of activity in the network was quantified in terms of ΔIFR_{SH} (ΔIFR averaged over the nodes of the stimulated hemisphere), and some representative trials of ΔIFR_{SH} are reported. The evoked area is obtained as the integral after stimulation (red line, between 0 and 500 ms) of ΔIFR_{SH} averaged across trials. Third (**bIII**), the SC-FC correlation and the evoked area are reported for different global couplings (i.e., a scaling factor of the SC), and both metrics reached a peak at G = 4 (working point). The dashed blue lines and arrows illustrate the matches between the FC and the SC maps for different G values. The dashed green lines and arrows illustrate the evoked area by the stimulus. (**cI**) We simulated control and local manipulation conditions. Local manipulations were implemented by silencing selected nodes. (**cII**) To assess the impact of local node silencing on spontaneous complexity, we calculated Lempel–Ziv complexity (LZc) on ongoing network activity. Furthermore, we separately stimulated different connectome nodes under different local manipulations and calculated the Perturbational Complexity Index (PCI) to gauge the impact of local silencing on the evoked activity.

2.1.3. Spontaneous Activity and Stimulation Protocol

For the analysis of spontaneous activity, each condition was run for 4000 s, and the time-series were split into 10 segments of 400 s.

On the other hand, to examine the model's evoked response, a square wave pulse of 5 ms and amplitude 1 was applied to a single connectome node, specifically targeting the excitatory pyramidal cells (as an additive term to Equation (1)). In our study, we individually stimulated a total of 12 nodes located in the right hemisphere (see Section 2.1.4 below for details), homogeneously sampling all cortical lobes (Table 1).

In all conditions (control and lesions) a stimulus was delivered to the same node (i.e., same stimulus) 500 times (500 trials) by reinitializing each simulation. We also jittered the onset of the stimulus within a range of 2 s. Note that in the Larter–Breakspear model, all quantities are dimensionless except for time [56], which allows a straight comparison with the experimental time courses.

Table 1. Labels of the cortical nodes and their description in Dconn. The stimulated nodes are reported in bold.

Label	Description
A1	Primary auditory cortex
A2	Secondary auditory cortex
Amyg	Amygdala
CCa	Anterior cingulate cortex
CCp	Posterior cingulate cortex
CCr	Retrosplenial cingulate cortex
CCs	Subgenual cingulate cortex
FEF	Frontal eye field
G	Gustatory area
HC	Hippocampal cortex
IA	Anterior insula
IP	**Posterior insula**
M1	Primary motor area
PCi	**Inferior parietal cortex**
PCip	**Cortex of intraparietal sulcus**
PCm	Medial parietal cortex (i.e. precuneus)
PCs	**Dorsal parietal cortex (superior parietal lobule)**
PFCcl	**Centrolateral prefrontal cortex**
PFCdl	**Dorsolateral prefrontal cortex**
PFCdm	Dorsomedial prefrontal cortex
PFCm	Medial prefrontal cortex
PFCorb	**Orbitofrontal cortex**
PFCpol	**Pole of prefrontal cortex**
PFCvl	Ventrolateral prefrontal cortex
PHC	Parahippocampal cortex
PMCdl	Dorsolateral premotor cortex
PMCm	**Medial premotor cortex (i.e. supplementary motor area)**
PMCvl	Ventrolateral premotor cortex
S1	Primary somatosensory cortex
S2	**Secondary somatosensory cortex**
TCc	**Central temporal cortex**
TCi	Inferior temporal cortex
TCpol	Pole of temporal cortex
TCs	Superior temporal cortex
TCv	Ventral temporal cortex
V1	Primary visual cortex
V2	**Secondary visual cortex**

2.1.4. Local Manipulation Modeling

Building upon prior modeling studies [38,40,61], we simulated local network alterations by reducing the excitability of selected nodes. This silencing was achieved by hyperpolarizing the manipulated nodes (Figure 1c) to an extent which completely suppresses their firing activity (mean firing rate = 0). To achieve this, we abolished the excitatory nonspecific input (ane = 0) and increased the nonspecific inhibitory input (ani = 0.6). We implemented the different manipulations in one hemisphere (the right hemisphere) to simulate an affected hemisphere and an intact one (left hemisphere). Consistent with empirical studies [27], we stimulated the affected hemisphere to assess cortical reactivity following perturbation near the silenced node.

In line with previous work where 5% of the nodes were lesioned [39], in our study each manipulation involved approximately 4% of the connectome nodes (three nodes). As in [39], each local manipulation was defined by first choosing a central node (center of the manipulation) to be silenced and then selecting the remaining nodes to silence based on a geometrical distance criterion (Euclidean distance) from the central node. Manipulation details are reported in Table 2. Whenever the stimulated and manipulated nodes overlap, the latter were replaced with the closest non-manipulated nodes to the center of the manipulation. For instance, when stimulating rPCip, which was also part of local manipulation 1 (L1), we spared rPCip and silenced the next closest node (rV2). For a fair comparison across conditions between spontaneous and evoked metrics, non-identical manipulations were excluded whenever a correlation was performed (e.g., in Table S4 in Supplementary Material).

Table 2. Local manipulation labels in the Dconn connectome. The labels of the local manipulations and the corresponding nodes silenced in the Dconn connectome. The ranking is based on the MFR difference (from lowest to highest). Note that when a stimulus overlaps with a silenced node (in bold), the latter is replaced by a nearby node.

Local Manipulation Label	Nodes	Ranking (MFR_Δ)
L1	**PCip, PCs**, PCm	10
L2	**PFCcl, PFCdl**, PMCvl	7
L3	**TCc**, TCs, TCi	4
L4	**V2**, V1, CCr	18
L5	CCs, **PFCorb**, Amyg	19
L6	CCa, CCp, CCr	13
L7	M1, S1, PMCdl	5
L8	PCm, **PCip**, CCp	15
L9	PFCdm, CCa, PFCm	11
L10	A1, A2, **S2**	16
L11	Amyg, PHC, CCs	17
L12	HC, PHC, TCv	2
L13	**PFCpol**, PFCm, PFCdm	9
L14	PFCvl, G, PMCvl	8
L15	TCpol, Amyg, **PFCorb**	20
L16	CCa, PFCdm, **PFCdl**	12
L17	IP, TCs, **S2**	14
L18	S1, M1, **PCs**	3
L19	**PFCdl**, CCa, **PFCcl**	6
L20	TCv, PHC, TCi	1

This procedure resulted in a total of 12 control conditions (stimulations without any node manipulation) and 240 manipulation conditions (silencing of 20 different nodes for each stimulation, 12×20).

2.1.5. Validation on a Larger Connectome (Hconn)

As a proof of concept aimed at confirming the validity of the observed findings, we repeated the analysis pertaining to PCI using a connectome endowed with finer parcellation (Hconn) consisting of 998 areas [48]. Hconn corresponds to a human connectome, with symmetric bidirectional connections, and has been used in several studies [39,51,56,62]. We tested a control condition and 20 local node manipulations, which are detailed in Table S3 (Supplementary Material). Each of them involved approximately 4% of the nodes (40 nodes), and the implementation procedure was the same as in Section 2.1.4 (with the only exception being that in Dconn, ani = 0.6, while in Hconn, ani = 0.65, as more inhibition was required to suppress firing activity). In Hconn, we limited the number of stimulations to one performed over a portion of the superior parietal cortex (SP, Table S1 in Supplementary Material) of the manipulated hemisphere. In particular, to maintain a comparable fraction of stimulated nodes with the Dconn connectome (1/76 = 0.013), a total of 14 nodes of SP were simultaneously stimulated (14/998 = 0.014) that were chosen based on their adjacency to a central node, following the same geometrical approach used in Section 2.1.4. As in Dconn, the stimulus was delivered 500 times (500 trials) in each condition (see Section 2.1.3).

2.2. Analysis of Network Simulations

2.2.1. Firing Activity Analysis

The first step of all analysis consisted in the detection of spiking activity of all nodes of the network. Spike timing was established as the passage of membrane potential of the nodes above a fixed threshold (-0.05, Figure 1a).

We defined the mean firing rate for each region/node of interest (MFR_{ROI}) as the amount of spikes divided by the time window of observation.

To characterize the global/population activity of the model (MFR), we averaged the MFR_{ROI} values across nodes (either all nodes or, when specified, the ones of the intact or the manipulated hemisphere):

$$\text{MFR} = \langle \text{MFR}_{\text{ROI}} \rangle_{\text{nodes}} \tag{8}$$

Then, to quantify the impact of the local manipulation on activity, we defined the MFR difference (MFR_Δ) as:

$$\text{MFR}_\Delta = \text{MFR}(\text{local manipulation}) - \text{MFR}(\text{control}) \tag{9}$$

where MFR(condition) refers to the MFR in a condition of interest. Note that the MFR_Δ involved only the nodes not affected by the local manipulation (i.e., excluding the silenced nodes also in the control condition).

Then, for each node we defined the time-dependent Instantaneous Firing Rate (IFR(t), in Hz) as the frequency of spikes in a time window of 25 ms, and the temporal dependence was obtained by sliding the time window by 10 ms on the simulated data. We varied the size of the time window (e.g., 50 ms) and found qualitatively similar results.

In order to quantify the impact of the stimulation on the node's activity, we defined the quantities:

$$\Delta \text{IFR}(t) = \text{IFR}(t, \text{trial}) - \langle \text{IFR}(t, \text{trial}) \rangle_{(t<0)} \tag{10}$$

$$\langle \Delta \text{IFR}(t) \rangle = \langle \Delta \text{IFR}(t, \text{trial}) \rangle_{\text{trials}} \tag{11}$$

where <IFR(t, trial)>$_{(t<0)}$ is the average IFR over the time prior to stimulation, and <ΔIFR(t)>$_{\text{trials}}$ is the average ΔIFR across trials.

The level of network synchrony was quantified through the averaged pairwise cross-correlation between the spontaneous IFR signals:

$$
CC_{IFR} = \left\langle \frac{Cov\left(IFR_i, IFR_j\right)}{\sigma(IFR_i)\, \sigma\left(IFR_j\right)} \right\rangle
\tag{12}
$$

where <...> denotes the average over all possible pairs of nodes (excluding silenced nodes), $Cov(IFR_i, IFR_j)$ is the covariance between two spontaneous IFR signals (IFR_i, IFR_j), and $\sigma(IFR_i)$, $\sigma(IFR_j)$ are the corresponding standard deviations of the IFR signals

2.2.2. Network Analysis

We employed graph metrics based on the weighted degree to assess the centrality of a node in the network [63]. In the Dconn connectome, we computed the weighted out-degree (WD) of each node (sum of weighted outgoing connections of a node) in order to analyze the relationship between network centrality and complexity index topographies (see below, Sections 2.2.3 and 2.2.4). Notice that in symmetrical graphs, such as Hconn and non-directional functional connectivity (see below), the out-degree of a node is equal to its in-degree.

We computed the same quantities on the spontaneous functional connectivity (FC) in the control condition. The strengths of the functional connections between node pairs were obtained as the pairwise Pearson's correlation coefficient between their spontaneous instantaneous firing rates (IFRs). In addition, to corroborate our findings, we computed the FC_{BOLD} on the BOLD signal, a widely used approach in the literature with this model [39,50,51,56–58]. The BOLD signal was estimated from the model's output following [39]. We used the nonlinear Balloon–Windkessel hemodynamic model [64], and the input to the model was the absolute value of the time derivative of the excitatory membrane potential within each node. All the hemodynamic parameters were taken from [64]. Lastly, the estimated BOLD signal was sampled every 2 s. The FC_{BOLD} is defined as the Pearson correlation coefficient between each pair of BOLD signals. Then, similar to the SC analysis, we used the WD from the FC_{IFR} and the FC_{BOLD} to investigate the relationship between node centrality and complexity topographies. We also conducted the analysis by performing global signal regression (GSR) on the BOLD signal [51].

2.2.3. Complexity Indices

- Lempel–Ziv Complexity

The spatiotemporal differentiation of the spontaneous instantaneous firing rate was calculated by the Lempel–Ziv complexity (LZc) [44]. The optimal time window to compute LZc was examined by selecting temporal segments of variable lengths (from 1 s to 800 s). LZc decreased when increasing the temporal segments and reached a plateau around 200 s, and starting from 400 s, the variability, quantified by the coefficient of variation (CV), was less than 0.0004. For each condition, we calculated LZc over 10 segments of spontaneous activity (400 s each) and reported its mean $\pm$ SD.

- Perturbational Complexity Index

The Perturbational Complexity Index (PCI) quantifies the spatiotemporal complexity of brain activity evoked by an external perturbation [17]. To compute PCI, we followed the procedure outlined in [17], with the notable difference that we applied it to the IFR time series of the brain nodes.

In short, the significant evoked activities of each node, with respect to baseline, were determined by applying a non-parametric permutation test to the IFR. The baseline activity (pre-stimulus, time window = [−1000, 0 ms]) was used to determine, for each node, thresholds of significance (significance level set to 0.01, 500 bootstraps) and accounting for multiple comparison testing using the maximum test statistic. In this way, we derived a spatiotemporal matrix of significant activity [SS(x,t)], where SS(x,t) = 1 for significant

activity in node x at time t, and SS(x,t) = 0 otherwise. The SS matrix was then sorted according to the amount of significant activity during the post-stimulus interval of each node (e.g., most/less active at the bottom/top rows). Then, the Lempel–Ziv complexity (CL) was calculated on the binary matrix [SS(x,t)] of the significant IFR (first 500 ms after the pulse).

Finally, PCI^{LZ} is defined as the normalized CL of the evoked spatiotemporal patterns SS(x,t):

$$PCI = CL \cdot \frac{\log_2(L)}{(L \cdot Hsrc(L))} \tag{13}$$

where L is the size of the matrix [SS(x,t)] (L = number of nodes $\times$ number of time samples), and Hsrc is the source entropy given by:

$$Hsrc(L) = -p_1 \cdot \log_2(p_1) - (1 - p_1) \cdot \log_2(1 - p_1) \tag{14}$$

where p_1 and $(1 - p_1)$ are the fraction of "1" (significant activity) and "0" (non-significant activity) in the binary matrix.

Spatial temporal maps were represented based on SS and the $<\Delta IFR(t)>$ (Equation (10)). In particular, for each time point t, the $\Delta IFR(t)$ of the nodes with significant activity (i.e., SS(., t) = 1) were reported.

In all conditions (control and manipulations), each stimulus was repeated 500 times. Then, 10 resamples of 300 trials (without repetitions) were formed, and the PCI was computed on each subgroup. We assessed the stability of PCI versus the number of trials (ranging from 10 to 500 trials) and observed that the PCI values reached a plateau around 200 trials, and starting from 300 trials, the variability (CV) was less than 0.01.

2.2.4. Complexity Topographies

The contribution of each node to the complexity indices used was investigated by performing linear regressions between the complexity values (LZc and PCI) and the spontaneous activity of each node (MFR$_{ROI}$) for different conditions (local manipulations and control). The coefficient of determination (R^2) for each node was then computed and mapped onto the brain topographies. Thus, LZc-R^2 and PCI-R^2 topographies were derived. Given the 12 stimulation sites for PCI, 12 topographies were generated, which were then averaged into a single PCI-$<R^2>$ topography.

2.2.5. Statistical Analysis

Statistical analyses were performed using Python 3.7, employing the SciPy (1.9.3), statsmodels (0.13.5), and scikit-posthocs (0.8.1) packages. The data are expressed as mean $\pm$ standard deviation (SD) unless otherwise indicated. The boxplots report the first and third quartiles (lower/upper line of the box), the mean of the distribution (horizontal line in the box), and the whiskers (5th and 95th percentiles). The data were checked for normal distribution and homogeneity of variance using Shapiro–Wilk test and Levene test, respectively. According to the results, either parametric (e.g., one-way ANOVA and *t*-test) or non-parametric (e.g., Kruskal–Wallis H-test and Dunn's test) tests were performed. *p* values were adjusted for multiple comparisons using the Benjamini–Hochberg method to control the false discovery rate. Multiple one-sample *t*-tests were conducted with Bonferroni–Holm *p*-values correction to test the impact of each local manipulation compared with the control. Linear correlation between the metrics was computed with the Pearson correlation coefficient and its associated two-sided *p*-value. We conducted simple and multivariate linear regressions, calculating the coefficient of determination (R^2, and $R^2_{adjusted}$ to account for multiple regressors) and the *p*-value of the F-statistic. Additionally, we computed the slope coefficients of the regressors and their corresponding two-sided 95% confidence intervals (95% CI). For all statistical analyses, alpha = 0.05.

3. Results

3.1. Spontaneous Activity

Impact of Local Node Silencing on Spontaneous Complexity Measures

We first investigated the impact of local silencing on the model's spontaneous activity by quantifying the mean firing rate difference (MFR_Δ) on the nodes within the manipulated hemisphere, the intact one, as well as in the entire model compared with the same nodes in the control condition (Figure 2a). This analysis revealed that the MFR decreased the most in the affected hemisphere ($MFR_\Delta = -3.621 \pm 1.629$ Hz, mean across all manipulations $\pm$ SD) and to a lesser extent in the intact hemisphere (-1.431 ± 0.992 Hz).
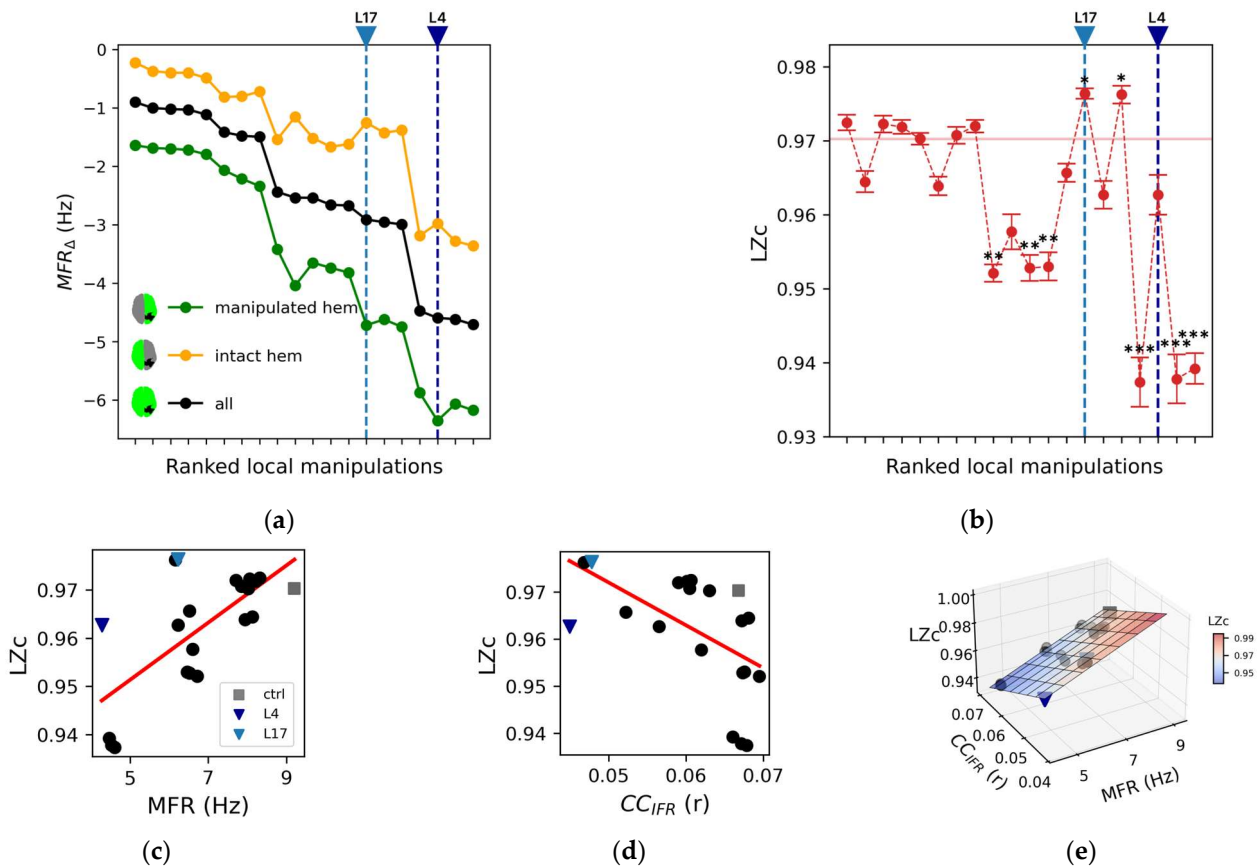
Figure 2. Impact of local manipulations on whole-brain spontaneous activity. (**a**) Mean firing rate difference (MFR_Δ, see Methods) for each silencing condition of the manipulated hemisphere (green), the intact one (yellow), and overall nodes (black). Note that the ranking (i.e., ranked local manipulations, see Table 2) is based on the black curve. (**b**) The Lempel–Ziv complexity (LZc) metric is reported versus the same ranked local manipulations. The red horizontal lines mark the average value of LZc in the control condition. Error bars represent one standard deviation and asterisks indicate a statistically significant difference from the control condition (* $p < 0.05$, ** $p < 0.01$, *** $p < 0.001$; Kruskal–Wallis and Dunn post hoc test with Benjamini–Hochberg correction). (**c**) Linear regressions relating the mean firing rate of all nodes (MFR) to LZc ($r = 0.69$; $p = 0.0005$). (**d**) Linear regression relating the averaged pairwise cross-correlation (CC_{IFR}) to LZc ($r = -0.55$, $p = 0.009$). (**e**) Multivariate regression of LZc with respect to the independent variables MFR and CC_{IFR} ($R^2 = 0.98$, $R^2_{adjusted} = 0.98$, $p = 2 \times 10^{-16}$).

We then quantified the impact of local node silencing on the complexity of spontaneous brain dynamics by computing Lempel–Ziv complexity (LZc) on the instantaneous firing rate (IFR) derived from the model time-series (Figure 2b). Notably, in 12 out of 20 local manipulations, LZc was not statistically different from control (Kruskal–Wallis and Dunn post hoc test with Benjamini–Hochberg correction). As a consequence, even though LZc

positively correlated with MFR (LZc: r = 0.69; *p* = 0.0005, Figure 2c), it did not reflect the changes of network complexity with respect to control condition.

Further exploring the network properties relevant for complexity, we computed the averaged pairwise cross-correlation (CC_{IFR}, see methods) between nodes as a measure of the synchrony of network interactions. CC_{IFR} was lower across local manipulations when compared to control (control: 0.067, average across manipulations: 0.061 ± 0.007; Figure 2d), which corresponds to a larger segregation of the network patterns. We found a negative correlation between LZc and CC_{IFR} (r = −0.55, *p* = 0.009; Figure 2d).

Considering the combined role of brain activity levels (MFR) and network interactions (CC_{IFR}) in shaping brain complexity, we performed a multivariate regression between MFR and CC_{IFR} in explaining LZc across all conditions (Figure 2e). This model effectively captured the variance of LZc ($R^2 = 0.98$, $R^2_{adjusted} = 0.98$, $p = 2 \times 10^{-16}$). Confirming the results obtained with the univariate analyses, a positive relationship was found for LZc with respect to MFR (slope coefficient, $\beta_{MFR} = 0.0072$, 95% CI [0.0066, 0.0078]), while CC_{IFR} was found to be negatively correlated with LZc ($\beta_{CC} = −1.2$, 95% CI [−1.3, −1.1]).

3.2. Evoked Activity

3.2.1. Local Node Silencing and PCI

We performed an extensive investigation of the responses to different stimuli for different node silencing within the connectome (12 stimuli × 20 manipulations). The impact of local node silencing on stimulus-evoked spatiotemporal activity was quantified by the Perturbational Complexity Index (PCI).

All manipulations caused a decrease of PCI with respect to the control condition (PCI_Δ) across stimuli (for each local manipulation *p* < 0.01, one sample *t*-test with Bonferroni–Holm correction; Figure 3a), albeit with a great variability depending on the specific stimulus-silencing pair (individual PCI values and statistical comparisons with respect to the control condition are reported in Figure S2).

In this respect, the responses of the model to stimulation of the right inferior parietal cortex (rPCi) for the control and two highly segregated local manipulations (L4 and L17, see Table 2 for a description of the manipulated nodes) serve as an illustrative example of such variability.

Specifically, the spatiotemporal distribution of the significant activities (see Methods) elicited by the stimulation pulse in the control and in the two representative manipulations displayed marked differences (Figure 3b). In particular, compared to the control condition, in the case of L4 silencing, the response was sustained in time but spatially redundant (i.e., the significant activities often involved the same areas), and it did not involve the non-stimulated hemisphere as confirmed by the <ΔIFR> temporal profile (Figure 3c top panel). On the other hand, in the case L17 silencing, significant evoked activity extended to the non-stimulated hemisphere (Figure 3c top panel) but was short-lived. The richness of the significant spatial-temporal patterns evoked by a stimulus can also be described by the SS matrices (see Methods, Figure 3c bottom panels). Compared to the control condition, the SS matrix of both L4 and L17 were either restricted in space (i.e., evoked activity remained more local, as in L4) or in time (i.e., the significant evoked activity decayed rapidly, as in L17). Interestingly, in L4, the significant activity described by the source entropy (Hsrc) was comparable to the control (0.79 ± 0.03 and 0.79 ± 0.02, respectively), but the evoked activity was more redundant in time (compare Figure 3a), confirming the dissociations between PCI and Hsrc (Supplementary Results, Section S2, Figure S3) also found in empirical studies [17]. Consistent with these observations, we found a significant reduction of PCI (*p* < 0.00001, ANOVA and post hoc pairwise T *t*-test with Benjamini–Hochberg correction) for both L4 and L17 (Figure S2, grey arrows. Control: 0.49 ± 0.03; L4: 0.25 ± 0.01; L17: 0.37 ± 0.04).

Furthermore, to corroborate our results, we performed a similar analysis with the more detailed connectome, Hconn (Figure S4A,B). Again, we found a significant reduction of PCI (Figure S4C) in all manipulation conditions (for each *p* < 0.000001, ANOVA and post hoc pairwise T *t*-test with Benjamini–Hochberg correction). The higher reduction of PCI

with Hconn compared to Dconn is likely due to a larger impact of node silencing on the local connectivity (i.e., areas surrounding the manipulation) as well as on the long-range connections reducing the communication between areas that are far apart.
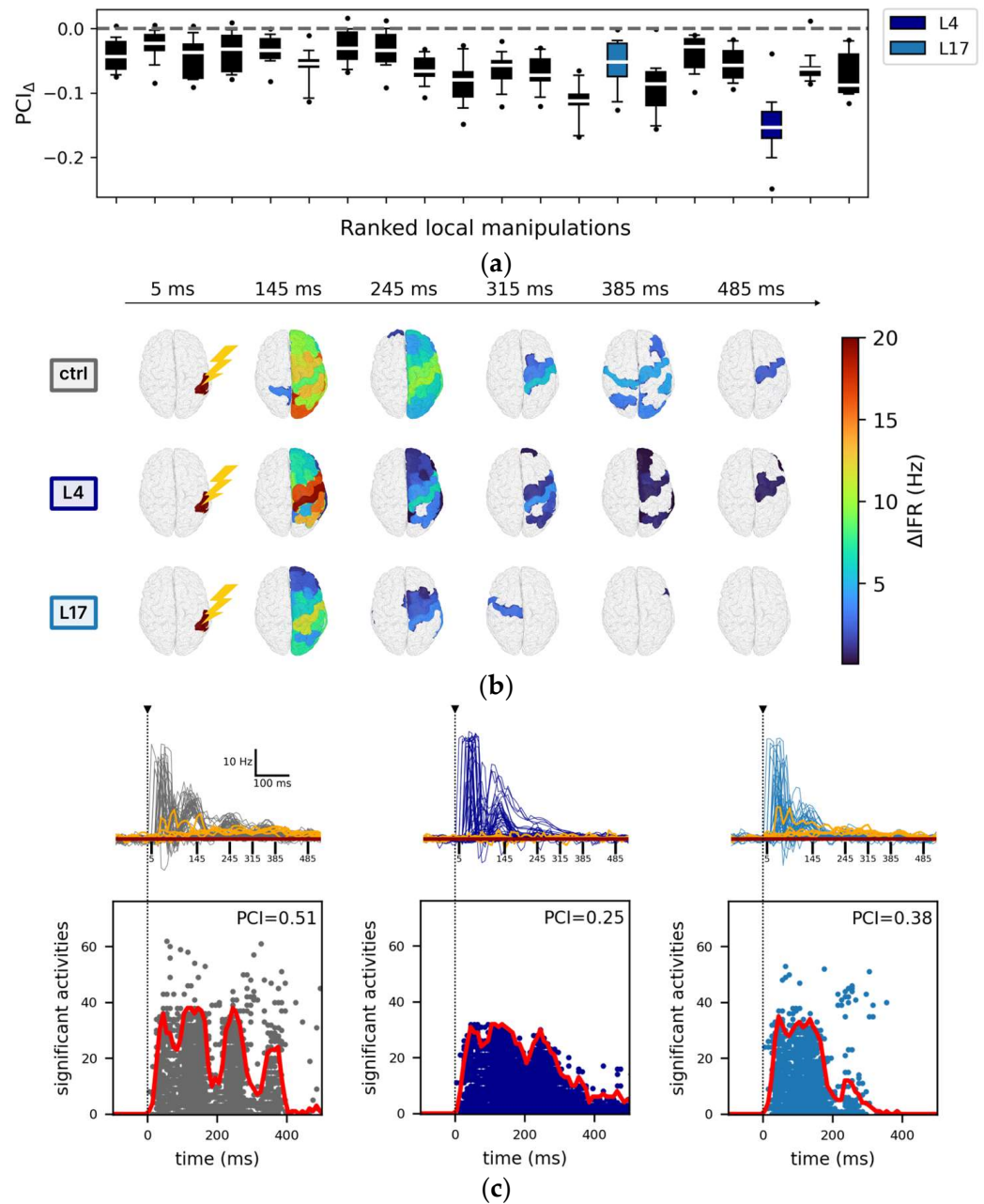

(a)

(b)

(c)

Figure 3. Impact of local manipulations on evoked activity. (**a**) Each box, corresponding to a local manipulation (ordered according to the ranking in Figure 2), displays the difference in PCI compared to the control (PCI$_\Delta$) for a given stimulation site (12 values per box, e.g., stimulation of rPCi: PCI$_\Delta$ (local manipulation) = <PCI$_{\text{local manipulation}}$> − <PCI$_{\text{ctrl}}$>, where <. . .> indicates mean across resamples). For each local manipulation, $p < 0.01$ (one sample t-test against mean zero with Bonferroni–Holm correction). (**b**) Spatiotemporal distribution of the areas with significant changes of their firing rate with respect to baseline activity following stimulation. Representative snapshots are reported at time t = 5 ms, t = 145 ms, t = 245 ms, t = 285 ms, t = 375 ms, and t = 485 ms in the control condition (top row), for the local manipulations L4 (middle row), and L17 (bottom row). (**c**) Top: the temporal courses of the instantaneous firing rate (<ΔIFR>) are reported for all nodes and separately for the representative conditions: ctrl (grey), L4 (dark blue), and L17 (light blue). For each condition,

the highest five <ΔIFR> (quantified as the total activity in the interval [0, 500] ms) of the non-stimulated hemisphere (orange traces) are also reported. The horizontal brown line indicates the mean baseline (defined as <ΔIFR(t)> averaged over the interval [−1000, 0] ms and over the latter highest five <ΔIFR(t)>). The vertical dotted black line marks the time of the stimulus, and the vertical continuous black lines are relative to the snapshots reported in panel b. Bottom: the corresponding sorted binary spatiotemporal matrices of significant activities highlight the impact of the local manipulations with respect to the control condition (the red line is the sum of significant activity over time). The Perturbational Complexity Index (PCI) decreases significantly ($p < 0.00001$, ANOVA and post hoc pairwise T test with Benjamini–Hochberg correction) in L4 and L17 compared with control (see Figure S2).

3.2.2. The Impact of Regional Silencing on PCI

By taking advantage of the systematic and extensive investigation of stimulation/silencing pairs, we further explored the variability of the impact of local silencing on both spontaneous and evoked metrics and investigated the contribution of individual region activity (i.e., MFR) to PCI across all conditions. Thus, for each stimulation, we performed a linear regression of the PCI values (i.e., mean across resamples) versus the spontaneous mean firing rate of a node/region of interest (MFR_{ROI}) across all conditions (including the control condition and all local manipulations). Figure 4a shows the linear regressions for two representative ROIs (right posterior cingulate cortex; rCCp and right parahippocampal cortex; rPHC), corresponding to the ROIs showing the third highest and third lowest average correlations across stimuli, respectively. For each of the two ROIs, we show two representative stimulations delivered to the inferior parietal cortex (PCi; $R^2 = 0.59$, $p = 5 \times 10^{-5}$ and $R^2 = 0.02$, $p = 0.58$) and the dorsolateral prefrontal cortex (PFCdl; $R^2 = 0.23$, $p = 0.03$ and $R^2 = 0.01$, $p = 0.60$). We found that PCI correlated well with MFR_{ROI} (CCp) for most stimulations (F-statistic of R^2, 11 with $p < 0.05$, one with $p = 0.051$), ranging from 0.19 to 0.59 (0.41 ± 0.14) (Figure 4b). On the other hand, MFR_{ROI} (PHC) was always non-significantly correlated with PCI across the 12 stimulations ($p > 0.05$).
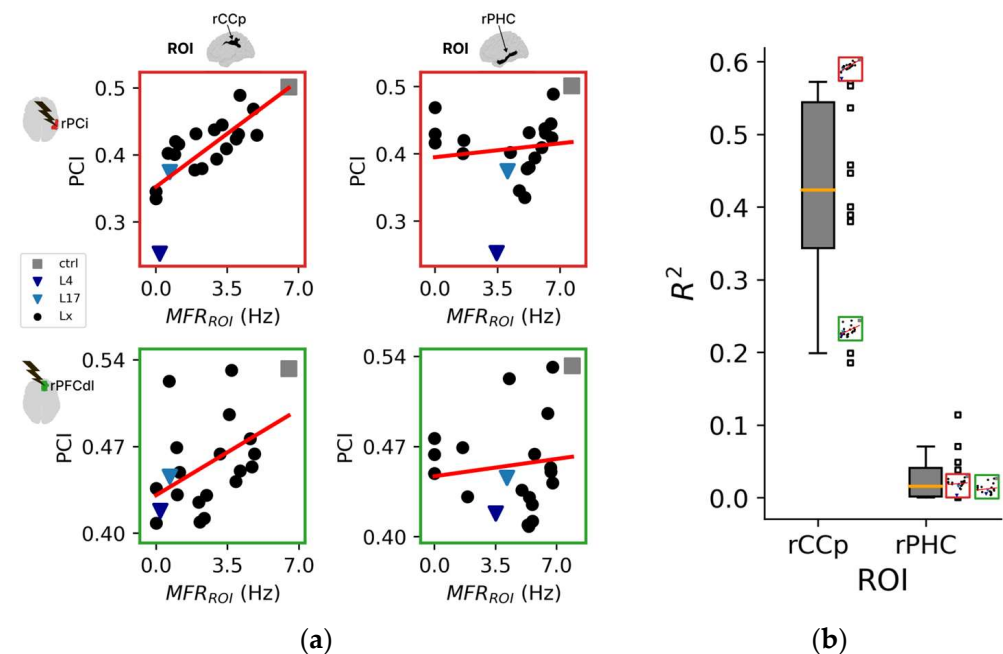

Figure 4. *Cont.*
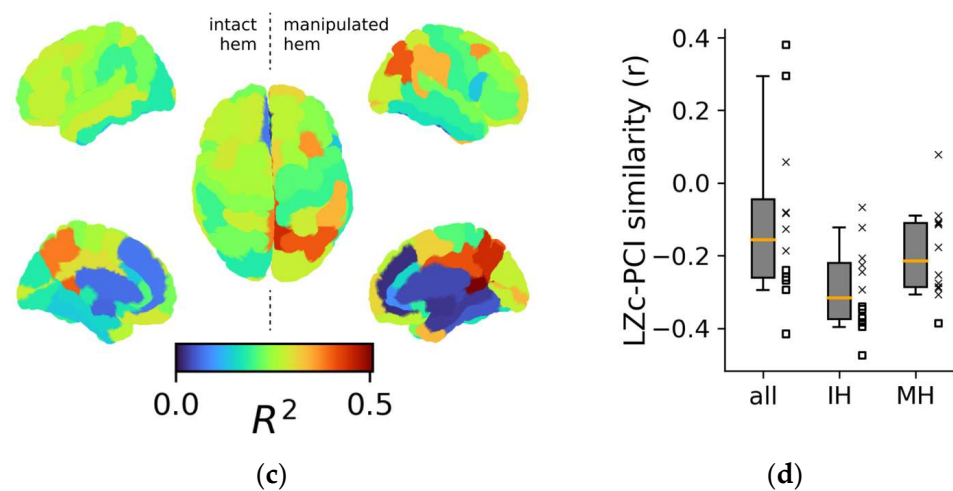
(**c**) (**d**)

Figure 4. Topological aspects of perturbational complexity. (**a**) Linear regressions relating PCI to the spontaneous mean firing rate of the ROIs/nodes rCCp and rPHC for two representative stimulation sites (red boxes: rPCi; green boxes: rPFCdl). (**b**) Boxplot of the R^2 relative to the PCI versus MFR_{ROI} (rCCp) and PCI versus MFR_{ROI} (rPHC) linear regressions for all stimulation sites. Note that the reduced plots of panel A are reported on the right of the boxplot to highlight the corresponding R^2 value. (**c**) Brain topography of the average R^2 across stimulation sites (<R^2>). For each ROI in the topography, the corresponding <R^2> is derived as in panel (**b**). (**d**) Distributions of the Pearson correlation coefficients computed across the R^2 topography maps of LZc with PCI and separately for all ROIs (all), intact hemisphere ROIs (IH), and manipulated hemisphere ROIs (MH). Each square and X symbol is relative to a stimulation site, and X markers indicate nonsignificant *p* values (>0.05).

The 12 regional maps of R^2 coefficients for each stimulation are presented topographically in Figure S5A, and the average topography across all stimulations is presented in Figure 4c. Interestingly, the three ROIs with the highest average R^2 across stimulations (i.e., CCr, <R^2> = 0.51 $\pm$ 0.13; PCm, <R^2> = 0.45 $\pm$ 0.14; CCp, <R^2> = 0.41 $\pm$ 0.14) were located in the posterior cortex of the manipulated hemisphere. In addition, the ROIs with the three highest R^2 values across all stimulations were predominantly located in the posterior regions (~89%, Figure S5B,C).

Consistently, we repeated the same analysis for the single stimulation on Hconn and found a similar regional specificity, with the highest R^2 values located in posterior regions of the manipulated hemisphere (Figure S4D).

3.2.3. Assessing Regional Similarity between Spontaneous and Evoked Complexity Metrics

We performed separate linear regressions for MFR_{ROI} versus LZc (Figure S6A,B) and computed the similarity between the R^2 topography maps of these and the 12 R^2 PCI topographies for each stimulation (Figure 4d). We found that the correlations between PCI and LZ topographies were anti-correlated (−0.1 $\pm$ 0.23), though many correlations were not significant (5 out of 12). Similar results were obtained when restricting the analysis to either the intact or the manipulated hemisphere (−0.29 $\pm$ 0.11 and −0.19 $\pm$ 0.12, respectively).

3.3. Assessing the Relationship between Complexity Measures and Graph Properties

We explored the relationship between the R^2-topographies derived from spontaneous (LZc) as well as perturbational complexity (PCI) measures and basic graph properties. To this aim, we correlated the weighted degree (WD) of each node (an index of network centrality calculated both on SC and FC) with the corresponding values of the complexity-R^2 topographies (Figure 5). The WD computed on the SC showed a weak, albeit significant, correlation with the PCI average-R^2 topography across the 12 stimulations (r = 0.34, *p* = 0.0026; Figure 5a). Conversely, we did not find a significant correlation with the LZc-R^2 topography (*p* = 0.063, Figure 5b). Similarly, we found a significant correlation between the

WD computed on the SC and the PCI-R^2 topography applied to Hconn (r = 0.44, p = 2·10^{-49}; Figure S7A). Further, we found even more robust correlations between WD calculated on FC and the average PCI-R^2 topography (r = 0.6, p = 10^{-8}, Figure 5c). Again, no significant relationship was found between WD and the LZc-R^2 topography (p = 0.5, Figure 5d). Similar results (Figure S7B–E) were obtained when using WD calculated on the FC derived from BOLD signals (FC$_{BOLD}$; see Section 2).
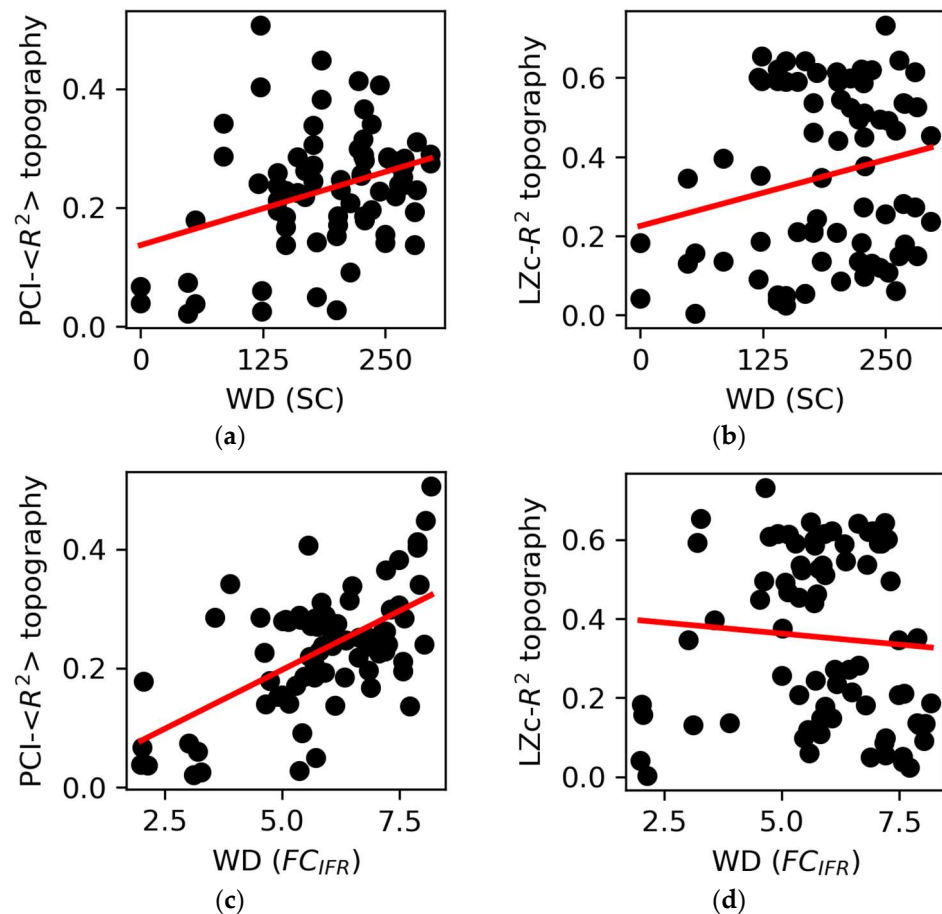

Figure 5. Graph properties and complexity topographies. (**a**) The weighted degree (WD) of structural connectivity (SC) nodes correlated with the PCI-<R^2> topography (r = 0.34, p = 0.0026) but (**b**) not with the LZc-R^2 topography (p = 0.063). (**c**) The WD of the nodes of the functional connectivity (FC$_{IFR}$) correlated with the PCI- <R^2> topography (r = 0.6, p = 10^{-8}) but (**d**) not with the LZc-R^2 topography (p = 0.5). Each point is representative of an ROI/node in the network. The regression lines are reported in red.

4. Discussion

The present study employed whole-brain computer simulations, systematic local manipulations (i.e., node silencing), and perturbations (i.e., brief pulses applied to local nodes) to assess the circuit-level properties underlying estimates of brain complexity. Our model has proved to be particularly suitable for investigating the mechanisms underlying brain complexity using various metrics commonly employed in empirical studies. In the present implementation, we were able to obtain spontaneous network activity as well as complex and enduring cortical interactions upon exogenous perturbations (Figure 1b), reminiscent of empirical observations [17,36]. Unlike in previous simulation works [33] and in line with experimental data, in the present model, brief local pulses were effective in evoking responses that propagated across distant nodes while spanning more prolonged time intervals. The presence of the non-linear NMDA current as implemented in the Larter

and Breakspear model [49] likely explains this important difference. Additionally, the same model has been shown to exhibit complex wave patterns, including traveling waves during spontaneous activity [56], thus arguably making it suitable for investigating complexity metrics that rely on activity propagation evoked by an external stimulus.

4.1. Impact of Local Silencing on Complexity Measures: The Role of Global Activity Levels and Network Dynamics/Interactions

All the local manipulations (i.e., node silencing) explored in this study showed an overall MFR decrease compared to the intact model (MFR_Δ), with a large variability depending on the manipulated nodes (Figure 2a). A similar trend was also observed for spontaneous complexity quantified with LZc, indicating a correlation between LZc and the global activity levels (MFR; Figure 2c). However, LZc often remained unchanged or even increased as compared to the control condition (Figure 2b), suggesting that the observed effects of local silencing on LZc were not merely explained by changes in global activity levels. Crucially, local manipulations resulting in a reduction of functional connectivity (i.e., segregation of network interactions) as captured by the correlation of activity across nodes (CC_{IFR}) tended to exhibit higher LZc values (Figure 2d). Thus, we tested the interplay between global activity levels (MFR) and network interactions (CC_{IFR}) in sustaining complex dynamics (LZc) through a 3D linear model (Figure 2e). This model, rooted in simple network activity variables, effectively described LZc, corroborating (1) the role of an optimal global activity level in shaping spontaneous complexity values and (2) the negative relationship of LZc with respect to network interactions. Importantly, this result underscores a significant limitation of various complexity metrics based on spontaneous activity, such as LZc, as they assume a priori network integration [6] and yield high values in systems composed of independent/segregated elements [41]. Here, we confirm, in a whole-brain connectome endowed with neural mass models, previous studies illustrating an imbalance of LZc towards network segregation [44].

A promising method to overcome this limitation and assess brain complexity, defined as the coexistence of integration and differentiation within a system, involves adopting a causal/perturbational approach [6]. This can be achieved empirically by employing local stimulations with TMS and estimating, with PCI, the information content of the causally generated interactions characterizing the integrated EEG response [17]. Unlike LZc, PCI is expected to decrease in systems with a loss of network interactions, given the restricted integrated response. Furthermore, PCI would be equally low in systems where the integrated response is redundant (i.e., undifferentiated), thus capturing an effective balance between functional integration and functional differentiation.

By the same token, in addition to the spontaneous complexity metric discussed above, we simulated this empirical approach by employing local perturbations (i.e., brief local pulses), extensively varying the stimulation site across different conditions (i.e., silencing different nodes). Each local manipulation had a detrimental effect on PCI, albeit with a heterogeneity influenced by the specific stimulus-silencing pair (Figure 3a and Figure S2). An even more substantial impact of local manipulations on PCI was found in Hconn (Figure S4A–C).

A marked difference between spontaneous and perturbational estimates of complexity was further confirmed by the lack of a correlation between LZc and PCI across conditions (Table S4). Such divergence, already observed in experimental studies [65,66], was particularly evident upon local manipulations leading to segregated network dynamics (reduced CC_{IFR}). This resulted in a less complex evoked response (as quantified by PCI; Figure 3b,c) despite increased LZc (Figure 2b). This result is also in line with several empirical findings across a variety of conditions where a disruption of effective connectivity across widespread brain networks results in a spatially constrained, short-lived EEG response to direct cortical stimulations with TMS and, in turn, in a significant reduction of PCI [17,18,25,67,68].

Overall, the comparison between LZc from spontaneous activity and PCI confirms that the latter more coherently hinges on an actual balance between functional integration and

functional differentiation. This intuition is further suggested by the 3D model relating MFR and CC_{IFR} applied to PCI. In this case, compared to LZc, the 3D model does not describe PCI values across conditions resulting in a slope coefficient for CC_{IFR} not significantly different from 0 for most stimulations (8 out of 12; Supplementary Results, Section S3).

4.2. Regional Aspects of Complexity Indices: The Role of Posterior Regions

We observed an association between complexity indices and global activity levels, highlighting the crucial role of suitable network activity in sustaining complex model dynamics (Table S4). However, we found a significant heterogeneity in how various local manipulations affected complexity, and this variation could not be straightforwardly accounted for by the global activity levels. As outlined in previous works [41], local, rather than global, activity features might underlie network complexity. Indeed, experimental EEG and fMRI studies conducted on humans, monkeys, and rats (during sleep, anesthesia, and following severe brain injuries) have linked the loss and recovery of consciousness to brain complexity based on the activity of posterior regions [69–71]. In this regard, a recent whole-brain modeling study [40] identified a few key nodes centered around the 'posterior hot zone' (i.e., precuneus and posterior cingulate cortex) that were pivotal for maintaining the model in an awake-like state. Reducing the activity of these nodes led to a shift in model dynamics, akin to unconscious states.

While LZc was largely explained by the activity of the most firing nodes irrespective of their spatial location (Supplementary Results, Section S4 and Figure S6), our model showed a similar dependency of PCI on the activity of posterior regions (Figure 4 and Figure S5). Specifically, our analysis revealed that the regional spontaneous activity (MFR_{ROI}) displaying the highest correlations with PCI included the retrosplenial cingulate cortex, the medial parietal cortex (precuneus), and the posterior cingulate cortex. Similar findings, encompassing a similar set of posterior regions, were found for the Hconn model (Figure S4D). These results nicely complement recent empirical observations involving rats under ketamine anesthesia [72], which found a strong correlation between PCI and activity in posteromedial regions. This study demonstrated that deactivation of these posteromedial regions was associated with disruptions in long-lasting and widespread cortical interactions following electrical stimulation. Altogether, these findings suggest the central hub role of posterior regions for long-range communications in cortical networks. Consistently, we have observed a positive correlation (Figure 5 and Figure S7) between the weighted degree (a metric quantifying hub centrality), particularly when applied to functional connectivity estimates (Figure 5c,d and Figure S7B,C) and the PCI-R^2 topographies (but not for LZc-R^2).

4.3. Limitations and Future Directions

This work represents a first attempt to characterize the large-scale determinants of brain complexity and to assess the relationship between observational and causal approaches towards its estimation. Given the intrinsic limitation imposed by in silico models of brain dynamics and by the use of surrogate estimates of brain complexity, more biophysically plausible node equations [32,73], as well as simulations including subcortical structures [74], should be considered for future implementations. In addition, the introduction of an appropriate forward model [75] to obtain EEG-level dynamics would allow for a more direct comparison between our findings and those obtained in empirical studies.

Along these lines, our implementation of the Hconn model (Figure S5) represents a proof of concept of the robustness of the observed findings tested on a connectome with a finer parcellation including short-range connections and serves as a promising springboard to expand the investigation to more realistic brain models such as vertex-based simulations [76].

Concerning the local manipulations conducted in this study, forthcoming research could incorporate alterations in local node dynamics that go beyond simply suppressing node activity. This could involve activity-dependent adaptation [34,77]. Indeed, in addition to the direct effect of the local silencing (either performed by activity or connectivity

manipulations), empirical evidence suggests the occurrence of an alteration in the activity of structurally intact cortical regions surrounding [78,79] or remotely connected [80] to the site of structural damage (i.e., regions with suppressed activity). Specifically, the activity of such regions switches to a sleep-like mode characterized by the tendency to display EEG slow waves. This activity is promptly revealed by direct cortical perturbations even when not directly present in the spontaneous EEG, thus confirming its activity-dependent nature [27,81,82]. Using a simple model, Cattani and colleagues [34] recently showed the key role of activity-dependent adaptation mechanisms in shaping the responses to perturbations and affecting the build-up of complex cortical interactions. Embedding such local alterations within a large-scale, connectome-based simulation, such as the one here implemented or similar [33,83], would allow one to more realistically simulate the large-scale network consequences of local node alterations.

4.4. Conclusions

Our work for the first time extensively integrates a perturbational approach with local node manipulations in a whole-brain computational model. This approximation marks an initial step towards a more detailed in silico exploration of the mechanisms behind the loss of brain complexity. Their translation may be relevant in real-world scenarios such as pathological conditions, as well as for therapeutic interventions aimed at recovering brain complexity.

Conflicts of Interest: The authors declare that they have no known competing financial interests or personal relationships that could have appeared to influence the work reported in this paper. Author Simone Sarasso is an advisor to Intrinsic Powers. Author Marcello Massimini is co-founder of Intrinsic Powers, a spin-off of the University of Milan, who provided funding and technical support for the work.

References

1. Tononi, G.; Sporns, O.; Edelman, G.M. A Measure for Brain Complexity: Relating Functional Segregation and Integration in the Nervous System. *Proc. Natl. Acad. Sci. USA* **1994**, *91*, 5033–5037. [CrossRef] [PubMed]
2. Deco, G.; Tononi, G.; Boly, M.; Kringelbach, M.L. Rethinking Segregation and Integration: Contributions of Whole-Brain Modelling. *Nat. Rev. Neurosci.* **2015**, *16*, 430–439. [CrossRef]
3. Bullmore, E.; Sporns, O. The Economy of Brain Network Organization. *Nat. Rev. Neurosci.* **2012**, *13*, 336–349. [CrossRef] [PubMed]
4. Sporns, O.; Tononi, G.; Edelman, G.M. Connectivity and Complexity: The Relationship between Neuroanatomy and Brain Dynamics. *Neural Netw.* **2000**, *13*, 909–922. [CrossRef] [PubMed]
5. Sporns, O. The Complex Brain: Connectivity, Dynamics, Information. *Trends Cogn. Sci.* **2022**, *26*, 1066–1067. [CrossRef] [PubMed]
6. Sarasso, S.; Casali, A.G.; Casarotto, S.; Rosanova, M.; Sinigaglia, C.; Massimini, M. Consciousness and Complexity: A Consilience of Evidence. *Neurosci. Conscious.* **2021**, *7*, niab023. [CrossRef]
7. Tononi, G.; Edelman, G.M. Consciousness and Complexity. *Science* **1998**, *282*, 1846–1851. [CrossRef]
8. Hagmann, P. *From Diffusion MRI to Brain Connectomics*; EPFL: Lausanne, Switzerland, 2005.
9. Sporns, O.; Tononi, G.; Kötter, R. The Human Connectome: A Structural Description of the Human Brain. *PLoS Comput. Biol.* **2005**, *1*, e42. [CrossRef]
10. Van Essen, D.C.; Smith, S.M.; Barch, D.M.; Behrens, T.E.J.; Yacoub, E.; Ugurbil, K. The WU-Minn Human Connectome Project: An Overview. *NeuroImage* **2013**, *80*, 62–79. [CrossRef]
11. Miller, K.L.; Alfaro-Almagro, F.; Bangerter, N.K.; Thomas, D.L.; Yacoub, E.; Xu, J.; Bartsch, A.J.; Jbabdi, S.; Sotiropoulos, S.N.; Andersson, J.L.R.; et al. Multimodal Population Brain Imaging in the UK Biobank Prospective Epidemiological Study. *Nat. Neurosci.* **2016**, *19*, 1523–1536. [CrossRef]
12. Kaiser, M. Connectomes: From a Sparsity of Networks to Large-Scale Databases. *Front. Neuroinformatics* **2023**, *17*, 1170337. [CrossRef] [PubMed]
13. Sanz Leon, P.; Knock, S.; Woodman, M.; Domide, L.; Mersmann, J.; McIntosh, A.; Jirsa, V. The Virtual Brain: A Simulator of Primate Brain Network Dynamics. *Front. Neuroinformatics* **2013**, *7*, 10. [CrossRef]
14. Breakspear, M. Dynamic Models of Large-Scale Brain Activity. *Nat. Neurosci.* **2017**, *20*, 340–352. [CrossRef] [PubMed]
15. Cakan, C.; Jajcay, N.; Obermayer, K. Neurolib: A Simulation Framework for Whole-Brain Neural Mass Modeling. *Cogn. Comput.* **2021**, *15*, 1132–1152. [CrossRef]
16. Lord, L.-D.; Stevner, A.B.; Deco, G.; Kringelbach, M.L. Understanding Principles of Integration and Segregation Using Whole-Brain Computational Connectomics: Implications for Neuropsychiatric Disorders. *Philos. Trans. R. Soc. A Math. Phys. Eng. Sci.* **2017**, *375*, 20160283. [CrossRef]
17. Casali, A.G.; Gosseries, O.; Rosanova, M.; Boly, M.; Sarasso, S.; Casali, K.R.; Casarotto, S.; Bruno, M.-A.; Laureys, S.; Tononi, G.; et al. A Theoretically Based Index of Consciousness Independent of Sensory Processing and Behavior. *Sci. Transl. Med.* **2013**, *5*, 198ra105. [CrossRef]
18. Casarotto, S.; Comanducci, A.; Rosanova, M.; Sarasso, S.; Fecchio, M.; Napolitani, M.; Pigorini, A.G.; Casali, A.; Trimarchi, P.D.; Boly, M.; et al. Stratification of Unresponsive Patients by an Independently Validated Index of Brain Complexity. *Ann. Neurol.* **2016**, *80*, 718–729. [CrossRef]
19. Timme, N.M.; Marshall, N.J.; Bennett, N.; Ripp, M.; Lautzenhiser, E.; Beggs, J.M. Criticality Maximizes Complexity in Neural Tissue. *Front. Physiol.* **2016**, *7*, 425. [CrossRef]
20. Colombi, I.; Nieus, T.; Massimini, M.; Chiappalone, M. Spontaneous and Perturbational Complexity in Cortical Cultures. *Brain Sci.* **2021**, *11*, 1453. [CrossRef]
21. Barbero-Castillo, A.; Mateos-Aparicio, P.; Porta, L.D.; Camassa, A.; Perez-Mendez, L.; Sanchez-Vives, M.V. Impact of GABAA and GABAB Inhibition on Cortical Dynamics and Perturbational Complexity during Synchronous and Desynchronized States. *J. Neurosci.* **2021**, *41*, 5029–5044. [CrossRef]
22. Arena, A.; Comolatti, R.; Thon, S.; Casali, A.G.; Storm, J.F. General Anesthesia Disrupts Complex Cortical Dynamics in Response to Intracranial Electrical Stimulation in Rats. *eNeuro* **2021**, *8*. [CrossRef] [PubMed]
23. Dasilva, M.; Camassa, A.; Navarro-Guzman, A.; Pazienti, A.; Perez-Mendez, L.; Zamora-López, G.; Mattia, M.; Sanchez-Vives, M.V. Modulation of Cortical Slow Oscillations and Complexity across Anesthesia Levels. *NeuroImage* **2021**, *224*, 117415. [CrossRef] [PubMed]

24. Cavelli, M.L.; Mao, R.; Findlay, G.; Driessen, K.; Bugnon, T.; Tononi, G.; Cirelli, C. Sleep/Wake Changes in Perturbational Complexity in Rats and Mice. *iScience* **2023**, *26*, 106186. [CrossRef] [PubMed]

25. Massimini, M.; Ferrarelli, F.; Huber, R.; Esser, S.K.; Singh, H.; Tononi, G. Breakdown of Cortical Effective Connectivity During Sleep. *Science* **2005**, *309*, 2228–2232. [CrossRef] [PubMed]

26. Ragazzoni, A.; Pirulli, C.; Veniero, D.; Feurra, M.; Cincotta, M.; Giovannelli, F.; Chiaramonti, R.; Lino, M.; Rossi, S.; Miniussi, C. Vegetative versus Minimally Conscious States: A Study Using TMS-EEG, Sensory and Event-Related Potentials. *PLoS ONE* **2013**, *8*, e57069. [CrossRef] [PubMed]

27. Sarasso, S.; D'Ambrosio, S.; Fecchio, M.; Casarotto, S.; Viganò, A.; Landi, C.; Mattavelli, G.; Gosseries, O.; Quarenghi, M.; Laureys, S.; et al. Local Sleep-like Cortical Reactivity in the Awake Brain after Focal Injury. *Brain* **2020**, *143*, 3672–3684. [CrossRef] [PubMed]

28. Sinitsyn, D.O.; Poydasheva, A.G.; Bakulin, I.S.; Legostaeva, L.A.; Iazeva, E.G.; Sergeev, D.V.; Sergeeva, A.N.; Kremneva, E.I.; Morozova, S.N.; Lagoda, D.Y.; et al. Detecting the Potential for Consciousness in Unresponsive Patients Using the Perturbational Complexity Index. *Brain Sci.* **2020**, *10*, 917. [CrossRef]

29. Usami, K.; Korzeniewska, A.; Matsumoto, R.; Kobayashi, K.; Hitomi, T.; Matsuhashi, M.; Kunieda, T.; Mikuni, N.; Kikuchi, T.; Yoshida, K.; et al. The Neural Tides of Sleep and Consciousness Revealed by Single-Pulse Electrical Brain Stimulation. *Sleep* **2019**, *42*, zsz050. [CrossRef]

30. Spiegler, A.; Hansen, E.C.A.; Bernard, C.; McIntosh, A.R.; Jirsa, V.K. Selective Activation of Resting-State Networks Following Focal Stimulation in a Connectome-Based Network Model of the Human Brain. *eNeuro* **2016**, *3*. [CrossRef]

31. Spiegler, A.; Abadchi, J.K.; Mohajerani, M.; Jirsa, V.K. In Silico Exploration of Mouse Brain Dynamics by Focal Stimulation Reflects the Organization of Functional Networks and Sensory Processing. *Netw. Neurosci.* **2020**, *4*, 807–851. [CrossRef]

32. Momi, D.; Wang, Z.; Griffiths, J.D. TMS-Evoked Responses Are Driven by Recurrent Large-Scale Network Dynamics. *Elife* **2023**, *12*, e83232. [CrossRef] [PubMed]

33. Goldman, J.S.; Kusch, L.; Aquilue, D.; Yalçınkaya, B.H.; Depannemaecker, D.; Ancourt, K.; Nghiem, T.-A.E.; Jirsa, V.; Destexhe, A. A Comprehensive Neural Simulation of Slow-Wave Sleep and Highly Responsive Wakefulness Dynamics. *Front. Comput. Neurosci.* **2023**, *16*, 1058957. [CrossRef] [PubMed]

34. Cattani, A.; Galluzzi, A.; Fecchio, M.; Pigorini, A.; Mattia, M.; Massimini, M. Adaptation Shapes Local Cortical Reactivity: From Bifurcation Diagram and Simulations to Human Physiological and Pathological Responses. *eNeuro* **2023**, *10*. [CrossRef] [PubMed]

35. Albert, R.; Jeong, H.; Barabási, A.-L. Error and Attack Tolerance of Complex Networks. *Nature* **2000**, *406*, 378–382. [CrossRef] [PubMed]

36. Seguin, C.; Sporns, O.; Zalesky, A. Brain Network Communication: Concepts, Models and Applications. *Nat. Rev. Neurosci.* **2023**, *24*, 557–574. [CrossRef] [PubMed]

37. Aerts, H.; Fias, W.; Caeyenberghs, K.; Marinazzo, D. Brain Networks under Attack: Robustness Properties and the Impact of Lesions. *Brain* **2016**, *139*, 3063–3083. [CrossRef]

38. Rabuffo, G.; Lokossou, H.-A.; Li, Z.; Ziaee-Mehr, A.; Hashemi, M.; Quilichini, P.P.; Ghestem, A.; Arab, O.; Esclapez, M.; Verma, P.; et al. Probing the Mechanisms of Global Brain Reconfiguration after Local Manipulations. *bioRxiv* **2023**, *2023*, 2023-09.

39. Alstott, J.; Breakspear, M.; Hagmann, P.; Cammoun, L.; Sporns, O. Modeling the Impact of Lesions in the Human Brain. *PLOS Comput. Biol.* **2009**, *5*, e1000408. [CrossRef]

40. Hahn, G.; Zamora-López, G.; Uhrig, L.; Tagliazucchi, E.; Laufs, H.; Mantini, D.; Kringelbach, M.L.; Jarraya, B.; Deco, G. Signature of Consciousness in Brain-Wide Synchronization Patterns of Monkey and Human fMRI Signals. *Neuroimage* **2021**, *226*, 117470. [CrossRef]

41. Koch, C.; Massimini, M.; Boly, M.; Tononi, G. Neural Correlates of Consciousness: Progress and Problems. *Nat. Rev. Neurosci.* **2016**, *17*, 307–321. [CrossRef]

42. Sanders, R.D.; Mostert, N.; Lindroth, H.; Tononi, G.; Sleigh, J. Is Consciousness Frontal? Two Perioperative Case Reports That Challenge That Concept. *Br. J. Anaesth.* **2018**, *121*, 330–332. [CrossRef] [PubMed]

43. Sanz-Leon, P.; Knock, S.A.; Spiegler, A.; Jirsa, V.K. Mathematical Framework for Large-Scale Brain Network Modeling in The Virtual Brain. *NeuroImage* **2015**, *111*, 385–430. [CrossRef] [PubMed]

44. Schartner, M.; Seth, A.; Noirhomme, Q.; Boly, M.; Bruno, M.-A.; Laureys, S.; Barrett, A. Complexity of Multi-Dimensional Spontaneous EEG Decreases during Propofol Induced General Anaesthesia. *PLoS ONE* **2015**, *10*, e0133532. [CrossRef] [PubMed]

45. Bullmore, E.; Sporns, O. Complex Brain Networks: Graph Theoretical Analysis of Structural and Functional Systems. *Nat. Rev. Neurosci.* **2009**, *10*, 186–198. [CrossRef]

46. Woodman, M.M.; Pezard, L.; Domide, L.; Knock, S.A.; Sanz-Leon, P.; Mersmann, J.; McIntosh, A.R.; Jirsa, V. Integrating Neuroinformatics Tools in TheVirtualBrain. *Front. Neuroinformatics* **2014**, *8*, 36. [CrossRef]

47. Kunze, T.; Hunold, A.; Haueisen, J.; Jirsa, V.; Spiegler, A. Transcranial Direct Current Stimulation Changes Resting State Functional Connectivity: A Large-Scale Brain Network Modeling Study. *NeuroImage* **2016**, *140*, 174–187. [CrossRef]

48. Hagmann, P.; Cammoun, L.; Gigandet, X.; Meuli, R.; Honey, C.J.; Wedeen, V.J.; Sporns, O. Mapping the Structural Core of Human Cerebral Cortex. *PLOS Biol.* **2008**, *6*, e159. [CrossRef]

49. Breakspear, M.; Terry, J.R.; Friston, K.J. Modulation of Excitatory Synaptic Coupling Facilitates Synchronization and Complex Dynamics in a Biophysical Model of Neuronal Dynamics. *Network* **2003**, *14*, 703–732. [CrossRef]

50. Honey, C.J.; Kötter, R.; Breakspear, M.; Sporns, O. Network Structure of Cerebral Cortex Shapes Functional Connectivity on Multiple Time Scales. *Proc. Natl. Acad. Sci. USA* **2007**, *104*, 10240–10245. [CrossRef]

51. Honey, C.J.; Sporns, O.; Cammoun, L.; Gigandet, X.; Thiran, J.P.; Meuli, R.; Hagmann, P. Predicting Human Resting-State Functional Connectivity from Structural Connectivity. *Proc. Natl. Acad. Sci. USA* **2009**, *106*, 2035–2040. [CrossRef]

52. Gollo, L.L.; Breakspear, M. The Frustrated Brain: From Dynamics on Motifs to Communities and Networks. *Philos. Trans. R. Soc. B Biol. Sci.* **2014**, *369*, 20130532. [CrossRef] [PubMed]

53. Gollo, L.L.; Mirasso, C.; Sporns, O.; Breakspear, M. Mechanisms of Zero-Lag Synchronization in Cortical Motifs. *PLOS Comput. Biol.* **2014**, *10*, e1003548. [CrossRef] [PubMed]

54. Gollo, L.L.; Zalesky, A.; Hutchison, R.M.; van den Heuvel, M.; Breakspear, M. Dwelling Quietly in the Rich Club: Brain Network Determinants of Slow Cortical Fluctuations. *Philos. Trans. R. Soc. B Biol. Sci.* **2015**, *370*, 20140165. [CrossRef] [PubMed]

55. Roberts, J.A.; Friston, K.J.; Breakspear, M. Clinical Applications of Stochastic Dynamic Models of the Brain, Part I: A Primer. *Biol. Psychiatry Cogn. Neurosci. Neuroimaging* **2017**, *2*, 216–224. [CrossRef] [PubMed]

56. Roberts, J.A.; Gollo, L.L.; Abeysuriya, R.G.; Roberts, G.; Mitchell, P.B.; Woolrich, M.W.; Breakspear, M. Metastable Brain Waves. *Nat. Commun.* **2019**, *10*, 1056. [CrossRef] [PubMed]

57. Endo, H.; Hiroe, N.; Yamashita, O. Evaluation of Resting Spatio-Temporal Dynamics of a Neural Mass Model Using Resting fMRI Connectivity and EEG Microstates. *Front. Comput. Neurosci.* **2020**, *13*, 91. [CrossRef] [PubMed]

58. Aquino, K.M.; Fulcher, B.; Oldham, S.; Parkes, L.; Gollo, L.; Deco, G.; Fornito, A. On the Intersection between Data Quality and Dynamical Modelling of Large-Scale fMRI Signals. *NeuroImage* **2022**, *256*, 119051. [CrossRef]

59. Honey, C.J.; Sporns, O. Dynamical Consequences of Lesions in Cortical Networks. *Hum. Brain Mapp.* **2008**, *29*, 802–809. [CrossRef]

60. Deco, G.; McIntosh, A.R.; Shen, K.; Hutchison, R.M.; Menon, R.S.; Everling, S.; Hagmann, P.; Jirsa, V.K. Identification of Optimal Structural Connectivity Using Functional Connectivity and Neural Modeling. *J. Neurosci.* **2014**, *34*, 7910–7916. [CrossRef]

61. Adhikari, M.H.; Raja Beharelle, A.; Griffa, A.; Hagmann, P.; Solodkin, A.; McIntosh, A.R.; Small, S.L.; Deco, G. Computational Modeling of Resting-State Activity Demonstrates Markers of Normalcy in Children with Prenatal or Perinatal Stroke. *J. Neurosci.* **2015**, *35*, 8914–8924. [CrossRef]

62. Tagliazucchi, E. The Signatures of Conscious Access and Its Phenomenology Are Consistent with Large-Scale Brain Communication at Criticality. *Conscious. Cogn.* **2017**, *55*, 136–147. [CrossRef] [PubMed]

63. Eryilmaz, H.; Pax, M.; O'Neill, A.G.; Vangel, M.; Diez, I.; Holt, D.J.; Camprodon, J.A.; Sepulcre, J.; Roffman, J.L. Network Hub Centrality and Working Memory Performance in Schizophrenia. *Schizophrenia* **2022**, *8*, 76. [CrossRef] [PubMed]

64. Friston, K.J.; Harrison, L.; Penny, W. Dynamic Causal Modelling. *NeuroImage* **2003**, *19*, 1273–1302. [CrossRef] [PubMed]

65. Farnes, N.; Juel, B.E.; Nilsen, A.S.; Romundstad, L.G.; Storm, J.F. Increased Signal Diversity/Complexity of Spontaneous EEG, but Not Evoked EEG Responses, in Ketamine-Induced Psychedelic State in Humans. *PLoS ONE* **2020**, *15*, e0242056. [CrossRef] [PubMed]

66. Ort, A.; Smallridge, J.W.; Sarasso, S.; Casarotto, S.; von Rotz, R.; Casanova, A.; Seifritz, E.; Preller, K.H.; Tononi, G.; Vollenweider, F.X. TMS-EEG and Resting-State EEG Applied to Altered States of Consciousness: Oscillations, Complexity, and Phenomenology. *iScience* **2023**, *26*. [CrossRef] [PubMed]

67. Ferrarelli, F.; Massimini, M.; Sarasso, S.; Casali, A.; Riedner, B.A.; Angelini, G.; Tononi, G.; Pearce, R.A. Breakdown in Cortical Effective Connectivity during Midazolam-Induced Loss of Consciousness. *Proc. Natl. Acad. Sci. USA* **2010**, *107*, 2681–2686. [CrossRef] [PubMed]

68. Bai, Y.; Xia, X.; Kang, J.; Yin, X.; Yang, Y.; He, J.; Li, X. Evaluating the Effect of Repetitive Transcranial Magnetic Stimulation on Disorders of Consciousness by Using TMS-EEG. *Front. Neurosci.* **2016**, *10*, 473. [CrossRef]

69. King, J.-R.; Sitt, J.D.; Faugeras, F.; Rohaut, B.; El Karoui, I.; Cohen, L.; Naccache, L.; Dehaene, S. Information Sharing in the Brain Indexes Consciousness in Noncommunicative Patients. *Curr. Biol.* **2013**, *23*, 1914–1919. [CrossRef]

70. Sitt, J.D.; King, J.-R.; El Karoui, I.; Rohaut, B.; Faugeras, F.; Gramfort, A.; Cohen, L.; Sigman, M.; Dehaene, S.; Naccache, L. Large Scale Screening of Neural Signatures of Consciousness in Patients in a Vegetative or Minimally Conscious State. *Brain* **2014**, *137*, 2258–2270. [CrossRef]

71. Luppi, A.I.; Craig, M.M.; Pappas, I.; Finoia, P.; Williams, G.B.; Allanson, J.; Pickard, J.D.; Owen, A.M.; Naci, L.; Menon, D.K.; et al. Consciousness-Specific Dynamic Interactions of Brain Integration and Functional Diversity. *Nat. Commun.* **2019**, *10*, 4616. [CrossRef]

72. Arena, A.; Juel, B.E.; Comolatti, R.; Thon, S.; Storm, J.F. Capacity for Consciousness under Ketamine Anaesthesia Is Selectively Associated with Activity in Posteromedial Cortex in Rats. *Neurosci. Conscious.* **2022**, *2022*, niac004. [CrossRef] [PubMed]

73. Bensaid, S.; Modolo, J.; Merlet, I.; Wendling, F.; Benquet, P. COALIA: A Computational Model of Human EEG for Consciousness Research. *Front. Syst. Neurosci.* **2019**, *13*, 59. [CrossRef] [PubMed]

74. Cabrera-Álvarez, J.; Doorn, N.; Maestú, F.; Susi, G. Modeling the Role of the Thalamus in Resting-State Functional Connectivity: Nature or Structure. *PLoS Comput. Biol.* **2023**, *19*, e1011007. [CrossRef] [PubMed]

75. Næss, S.; Halnes, G.; Hagen, E.; Hagler, D.J.; Dale, A.M.; Einevoll, G.T.; Ness, T.V. Biophysically Detailed Forward Modeling of the Neural Origin of EEG and MEG Signals. *NeuroImage* **2021**, *225*, 117467. [CrossRef]

76. Spiegler, A.; Jirsa, V. Systematic Approximations of Neural Fields through Networks of Neural Masses in the Virtual Brain. *NeuroImage* **2013**, *83*, 704–725. [CrossRef] [PubMed]

77. Cakan, C.; Obermayer, K. Biophysically Grounded Mean-Field Models of Neural Populations under Electrical Stimulation. *PLoS Comput. Biol.* **2020**, *16*, e1007822. [CrossRef]

78. Walter, W.G. The Electro-Encephalogram in Cases of Cerebral Tumour. *Proc. R. Soc. Med.* **1937**, *30*, 579–598. [CrossRef]

79. Nuwer, M.R.; Jordan, S.E.; Ahn, S.S. Evaluation of Stroke Using EEG Frequency Analysis and Topographic Mapping. *Neurology* **1987**, *37*, 1153–1159. [CrossRef] [PubMed]

80. Russo, S.; Pigorini, A.; Mikulan, E.; Sarasso, S.; Rubino, A.; Zauli, F.M.; Parmigiani, S.; d'Orio, P.; Cattani, A.; Francione, S.; et al. Focal Lesions Induce Large-Scale Percolation of Sleep-like Intracerebral Activity in Awake Humans. *NeuroImage* **2021**, *234*, 117964. [CrossRef]

81. Tscherpel, C.; Dern, S.; Hensel, L.; Ziemann, U.; Fink, G.R.; Grefkes, C. Brain Responsivity Provides an Individual Readout for Motor Recovery after Stroke. *Brain* **2020**, *143*, 1873–1888. [CrossRef]

82. D'Ambrosio, S.; Certo, F.; Bernardelli, L.; Pini, L.; Corbetta, M.; Pantoni, L.; Massimini, M.; Sarasso, S. Detecting Cortical Reactivity Alterations Induced by Structural Disconnection in Subcortical Stroke. *Clin. Neurophysiol.* **2023**, *156*, 1–3. [CrossRef] [PubMed]

83. Cakan, C.; Dimulescu, C.; Khakimova, L.; Obst, D.; Flöel, A.; Obermayer, K. Spatiotemporal Patterns of Adaptation-Induced Slow Oscillations in a Whole-Brain Model of Slow-Wave Sleep. *Front. Comput. Neurosci.* **2022**, *15*, 800101. [CrossRef] [PubMed]